A Quantitative, Topological Model of Reconnection and Flux Rope Formation in a Two-Ribbon Flare

D.W. Longcope and C. Beveridge

Department of Physics, Montana State University
Bozeman, Montana

Draft: February 2, 2007

ABSTRACT

We present a topological model for energy storage and subsequent release in a sheared arcade of either infinite or finite extent. This provides a quantitative picture of a twisted flux rope produced through reconnection in a two-ribbon flare. It quantifies relationships between the initial shear, the amount of flux reconnected and the total toroidal flux in the twisted rope. The model predicts reconnection occurring in a sequence which progresses upward even if the reconnection sites themselves do not move. While some of the field lines created through reconnection are shorter, and less sheared across the polarity inversion line, reconnection also produces a significant number of field lines with shear even greater than that imposed by the photospheric motion. The most highly sheared of these is the overlying flux rope. Since it is produced by a sequence of reconnections, the flux rope has twist far in excess of that introduced into the arcade through shear motions. The energy storage agrees well with previous calculations using the full equations of magnetohydrodynamics, and the agreement improves as the topology is defined using increasingly finer detail. This is the first comparative study of the application of a topological model to a continuous flux distribution. As such it demonstrates how the coarseness with which the photospheric flux distribution is partitioned affects the accuracy of prediction in topological models.

Subject headings: MHD — Sun: corona — Sun: magnetic fields — Sun: flares

1. Introduction

The two-ribbon flare is one of the most well-studied types of solar activity. The standard picture of this phenomena combines models of Carmichael (1964), Sturrock (1968), Hirayama

(1974) and Kopp & Pneuman (1976), and is now generally called the CSHKP model. Magnetic energy is stored when an arcade of field lines overlying a photospheric polarity inversion line (PIL) is sheared by photospheric motion. The shear is later released by reconnection at a coronal X-point in a current sheet (CS) as depicted in Figure 1. This creates low-lying closed field lines (C) and a disconnected plasmoid (P) whose ejection forms a coronal mass ejection (CME). The recently reconnected field lines map down to chromospheric ribbons (R) which appear to separate during the ongoing reconnection, the characteristic behavior observed during a flare.

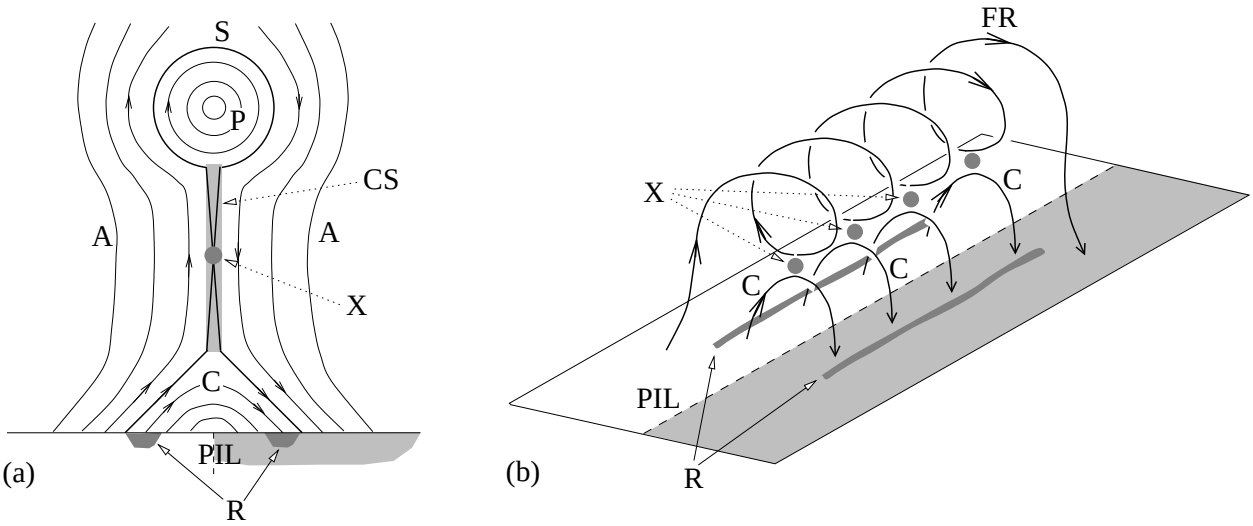

Fig. 1.— Basic elements of the CSHKP two-ribbon flare model in two (a) and three (b) dimensions. Expanded arcade field lines (A) are separated by a current sheet (CS). They reconnect at a magnetic X-point (X) to create closed field lines (C) and a plasmoid (P). The energy released by reconnection creates chromospheric flare ribbons (R) on either side of the PIL, just inside the separatrix (S). In the three-dimensional version (b) reconnection occurs at several sites (X) to create closed field lines (C) and a twisted flux rope (FR) instead of the plasmoid.

In spite of the broad acceptance of the CSHKP model, a potentially quantitative generalization of it to three dimensions is not yet widely accepted. A possibility, proposed by Gosling (1990) and depicted on the right of Figure 1, invokes reconnection at multiple sites (X) to form a twisted flux rope (FR) connected to the ends of the photospheric flux bands. This picture serves to link the two-ribbon flare with the creation of a twisted flux rope similar to those believed to be magnetic clouds (Burlaga et al. 1981) observed in *in situ* data. Without a more detailed and quantitative model, however, it is not possible to understand how much flare reconnection is required to produce a flux rope of specific axial flux or degree of twist. Recent observations (Qiu et al. 2007) point to relationships between

these quantities, but lacking a model it is unclear what form of relationship we might expect under a CSHKP-type picture.

In this work we present a quantitative, three-dimensional model of a scenario like that on the right of Figure 1. We use a topological formalism called the Minimum Current Corona (MCC, Longcope 1996; Longcope & Magara 2004), whereby reconnection along separators releases stored magnetic energy. The quantitative aspect of the MCC lies in its prediction of energy storage due to photospheric motion and of energy release from reconnection electric fields. Our application to a sheared arcade thereby provides a prediction of the relationships between shear, energy storage, magnetic reconnection and flux and twist in the resulting flux rope.

The MCC categorizes coronal field lines according to the connections they make between distinct photospheric source regions. This categorization is natural when the photospheric field consists of distinct concentrations, such as sunspots or quiet Sun magnetic elements. Applying the MCC to a continuous distribution, however, requires that it be somehow partitioned into distinct regions. In cases with extremely smooth flux distribution, such as the parallel bands anchoring an arcade, this partitioning can be somewhat arbitrary, and many different models are possible. It can be shown theoretically that each model provides a lower bound on the energy of the actual (continuous) magnetic field, and that the actual magnetohydrodynamic (MHD) energy is recovered in the limit of infinitely fine partitioning (Longcope 2001). This fact provides the basis for our application of the MCC to a sheared arcade.

Through comparisons to previous sheared arcade studies the present work yields the first investigation into the effect of partitioning on the quantitative predictions of the MCC. In previous, two-dimensional studies, a straight PIL separates bands of opposing photospheric flux. The bands, containing flux per unit length Φ', are separated by distance a. Displacing the two bands in opposite directions, parallel to the PIL, shears the arcade by an amount S defined as the ratio of relative parallel displacement to separation a (Klimchuk et al. 1988).

In numerical simulations (Mikic et al. 1988; Biskamp & Welter 1989; Klimchuk et al. 1988; Choe & Lee 1996), bands of flux with particular distributions were slowly sheared by parallel velocities of prescribed profile. If the motion is slow enough the coronal field will progress through a sequence of force-free equilibria with ever increasing energies. Although some simulations used periodic boundary conditions (Mikic et al. 1988; Biskamp & Welter 1989) others, notably Klimchuk et al. (1988) and Choe & Lee (1996), considered isolated bands of positive and negative flux. Klimchuk et al. (1988) found that the free energy stored in the stressed field was well approximated by the empirical relationship

$$\Delta W \;=\; W_{\rm pot}\, c_1 \ln(1 + c_2 S^2) \quad , \tag{1}$$

where $W_{\rm pot}$ is the energy of the unstressed (potential) field and the parameters $c_1 \simeq 0.7684$ and $c_2 \simeq 0.5530$ were found by fitting a range of different Gaussian flux profiles. This expression, which also matches simulations with Lorentzian flux profiles (Choe & Lee 1996), will be used for comparison to the topological model.

The continuous flux bands are partitioned by simply breaking them into into source regions of equal length, Δx, containing equal flux $\psi_0 = \Phi' \Delta x$. Different choices of region length constitute different partitions and the limit $\Delta x \to 0$ recovers a model with continuous, but very narrow, bands of photospheric flux.

We use this method to produce MCC models of sheared arcades which are all necessarily three-dimensional. Models in which the arcade is infinitely long are closest to the two-dimensional ideal on which Equation (1) is based. Restricting the flux bands to a finite length L, however, results in a genuinely three-dimensional model resembling the picture of Gosling (1990). We find that only this model can be used to predict the reconnection sequence required to release the stored energy. Naturally it is also the only one capable of predicting the relationship between flare-reconnection and the axial flux of the ejected flux rope.

The paper is organized as follows. The next section presents the MCC model of the infinite arcade with various partitions (i.e. values of $\Delta x/a$). It is demonstrated there that the MCC model follows the prediction of Klimchuk et al. (1988), Equation (1), and becomes increasingly accurate as $\Delta x \to 0$. Section 3 shows how restricting the flux bands to finite length L affects the topology of the model field. We illustrate this primarily with bands of length $L = 4a$ but consider, once again, a range of $\Delta x/a$. The following section then calculates the energy storage of these finite-length models. We illustrate a method for deriving the sequence of magnetic reconnection required to release the energy. This sequence progresses upward and leads ultimately to a flux rope with many more twists than the active region from which it came. In the final section we describe how this topological model relates to observed two-ribbon flares.

2. Two-dimensional (Infinite) Sheared Arcades

Our topological model of sheared arcades begins with two infinite lines of source regions each of which contains flux ψ_0 as described in the previous section. The regions in one line are separated from one another by Δx and the lines from one another by a. These are the partitioned representation of bands of photospheric flux $\Phi' = \psi_0/\Delta x$ per unit length, as shown in Figure 2.

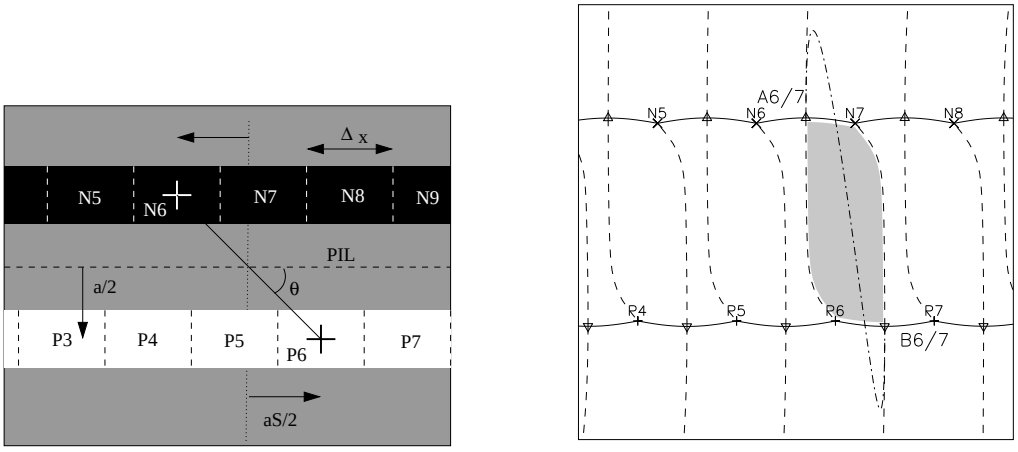

Fig. 2.— A topological model of an infinite arcade. (Left) Bands of of negative (black) and positive (white) flux separated by a across the PIL (dashed). These are partitioned into segments of length Δx. The arcade is sheared by displacing positive flux rightward and negative flux leftward, each by a distance of $aS/2$. Pairs of sources which were originally opposite across the PIL, such as $P6$ and $N6$, now make an angle $\theta = \cot^{-1}(S)$ with the PIL. (Right) The footprint of the potential field above the sheared arcade. The source centroids are denoted with +s and ×s and photospheric null points by $\bigtriangledown$s (positive null points) and $\bigtriangleup$s (negative null points). The spines and fan-traces from each null point are denoted by solid and dashed curves respectively. These divide the photosphere into regions which are the footprints of flux domains. The footprint of domain $P6$–$N7$ is shaded. Above it lies a separator field line linking null points $A6/7$ to $B6/7$ (labeled). Identical separators (not shown) occur in an infinite sequence stretching leftward and rightward.

The MCC depends on quantifying the amount of flux interconnecting each pair of sources. Field lines connecting a given pair form a distinct class called a *domain*. Opposing regions which are initially close to one another will be interconnected by large amounts of flux. Shearing the flux bands will move those regions in opposite directions, separating them and stretching the coronal field lines interconnecting them. This is the basis of energy storage in topological field models.

Quantifying interconnections requires knowledge of the entire coronal field above the photospheric source regions. Details of the flux distribution within a region will be less significant further and further from that region. Since a given region is unipolar we can express its field in a multipolar expansion whose first term will be a monopole. The first two terms in the series, monopole and dipole, are matched by a point source located at the region's flux-weighted centroid. This is the construction by which we will quantify the interconnections between flux regions. Figure 2 indicates how a set of rectangular source regions (left) is modeled by point sources (right).

In the initial configuration positive and negative sources face each other across the PIL and are labeled with the same index, such as $P6$ and $N6$ in Figure 2. The potential field contains, between every adjacent pair of sources, a prone null of the same sign whose spines connect to the sources. Thus between $P6$ and $P7$ lies a positive null point, which we designate $B6/7$, whose fan surface forms the separatrix between those two sources (see Figure 2).

The arcade is sheared by displacing positive sources one way and negatives the opposite way. A shear of magnitude S is achieved by a relative displacement of aS, as shown in the left panel of Figure 2. In the initial configuration each source is connected entirely to the corresponding element on the opposite side of the PIL: $P6$ connects entirely to $N6$ and so on. Barring any reconnection these connections will be maintained even as the sources separate.

The energy storage resulting from separating the connected sources can be estimated using the MCC (Longcope 1996; Longcope & Magara 2004) beginning with the potential magnetic field corresponding to the the present photospheric flux distribution. For the distribution shown in Figure 2 the potential field includes new connections to sources on the right looking across the PIL. An example of such a domain, indicated by shading in Figure 2, connects region $P6$ to $N7$. These new connections are topologically separated from the old ones ($P6$–$N6$ and $P7$–$N7$) by the fan surfaces originating in null points $A6/7$ and $B6/7$. These separatrices intersect along a magnetic separator which therefore encloses all flux connecting $P6$ to $N7$ and links the null points.

The net flux within domain Pi–Nj is denoted Ψ_{i-j} and by $\Psi^{(\mathrm{v})}_{i-j}$ when the potential

field is used. We know that $\Psi^{(\mathrm{v})}_{6-7} = 0$ when $S = 0$, since $P6$ is connected entirely to $N6$ by the potential field. When $S = \Delta x/a$ the bands will have been displaced by one complete interval, Δx, and source $P6$ will be directly across from $N7$. The potential field will be identical to the initial one except that $P6$ and $N7$ will now share all their flux: $\Psi^{(\mathrm{v})}_{6-7} = \psi_0$. We expect a smooth transition between these two extremes, such as

$$\Psi^{(\mathrm{v})}_{6-7} \simeq S\frac{a}{\Delta x}\psi_0 \;=\; Sa\Phi' \quad . \tag{2}$$

The situation will be the same for the identical separators to the left and right all along the arcade.

As a result of the photospheric shear, the potential field experiences flux transfer from domains such as $P6$–$N6$ into neighboring domains such as $P6$–$N7$. As the actual coronal field responds, without reconnection, it will not permit such flux transfer. This constraint prevents the field from achieving a potential state, and therefore requires that magnetic energy be stored in the field. To estimate the stored energy we seek the state of minimum magnetic energy subject to constraints on the fluxes of all interconnections; this is the so-called Flux Constrained Equilibrium (FCE). It turns out (Longcope 2001) that the minimizing magnetic field is current-free everywhere except for singular current layers (current ribbons) along the separators. This is *not* the actual field the system will achieve, however, it places a lower bound on the stored energy. In particular, the FCE is the lowest energy state for which the field is connected at an angle $\cot^{-1}(S)$ across the PIL.

The FCE can be approximated by adding to the separators *of the potential field*, the current required to prevent any change in the fluxes they enclose (Longcope & Magara 2004). The separator enclosing domain $P6$–$N7$, for example, would carry a current whose self-flux canceled out $\Psi^{(\mathrm{v})}_{6-7}$. Due to the symmetry of the infinite arcade all other separators will carry an equal current; we return to the more general situation in §4. These other currents will produce some flux through the $A6/7$–$B6/7$ separator as well. We demand that these two contributions produce a flux equal and opposite to that present in the potential field alone

$$\frac{I}{c}L\,\ln(eI^\star/|I|) \;+\; \tilde{M}\,\frac{I}{c} \;=\; -\,\Psi^{(\mathrm{v})}, \tag{3}$$

where L is the length of the separator, $I^\star$ is a measure of perpendicular magnetic shear (Longcope & Magara 2004) and $\tilde{M}$ is the sum of mutual inductances with all other separators. The last factor consists of a sum over an infinite number of currents, but their contribution ultimately falls off with the cube of distance so the sum converges. We describe in an appendix how we approximate this sum for this infinite arcade.

We performed a series of numerical experiments wherein arcades characterized by different ratios of $\Delta x/a$ were sheared. Each flux band in our experiments consisted of 11 sources,

and we calculated $\Psi^{(\mathrm{v})}$ from a single separator far from the effects of either end. The mutual inductance, $\tilde{M}$, was calculated, as described in the appendix, by summing over at least 30 identical separators. Equation (3) was solved at various values of shear, S, for each case. Figure 3 shows the results of the experiments. The current increases almost linearly with S in every case. Indeed, the relationship seems to depend very little on the coarseness with which the flux bands are resolved. This is somewhat surprising in view of the fact that $I^{\star}$, L and $\tilde{M}$ all vary substantially with $\Delta x/a$.

The separator currents in the MCC are the direct result of photospheric shearing. While they flow across the PIL at a relatively large angle, they are in fact the MCC representation of the current under the expanding arcade in the traditional MHD model system. In both systems the net current scales as $I \sim S\Phi'$ for small shear parameters (Klimchuk et al. 1988). The current is positive by convention since it flows parallel to the magnetic field in the separator. Along the separator shown in Figure 2 current flows from $B6/7$ to $A6/7$. This creates a self-flux directed underneath in the direction from $N7$ to $P6$: the sense opposite to the potential field. Currents flowing on parallel separators, say from $B5/6$ to $A5/6$, will also serve to offset the potential flux through separator $B6/7$–$A6/7$.

The chief benefit of the MCC model is that it provides an estimate of free energy storage. Integrating the non-potential flux from Equation (3) with respect to current I provides the electromagnetic energy stored in that particular separator. Dividing by the spacing between separators, Δx, yields the energy per length of arcade, plotted in the lower panel of Figure 3.

In order to compare this with the relation of Klimchuk et al. (1988), we need an expression for the energy of the potential field, W_{pot}. The potential-field energy of the continuous field depends on the flux profile within the bands. In general, it takes the form

$$\frac{W_{\mathrm{pot}}}{L} \;=\; \frac{K}{8\pi}\,(\Phi')^2 \quad , \tag{4}$$

where the dimensionless constant K depends on the profile. Gaussian and Lorentzian profiles used by Klimchuk et al. (1988) and Choe & Lee (1996), respectively, are characterized by $K = 1$ and $K = \pi/4$. For other smooth profiles in which positive and negative fluxes are distributed within bands of width comparable to their separation, K will be of order unity. On the other hand, when the flux is confined within a band much narrower than the separation, K will increase logarithmically with the ratio of these disparate scales.

The MCC calculates the free energy without direct reference to the potential energy of the field. For comparison to expression (1), however, it is necessary to find the energy of the potential field. Since the MCC is estimating the free energy of a field anchored to a continuous photospheric flux distribution we should use the potential energy of *that*, rather

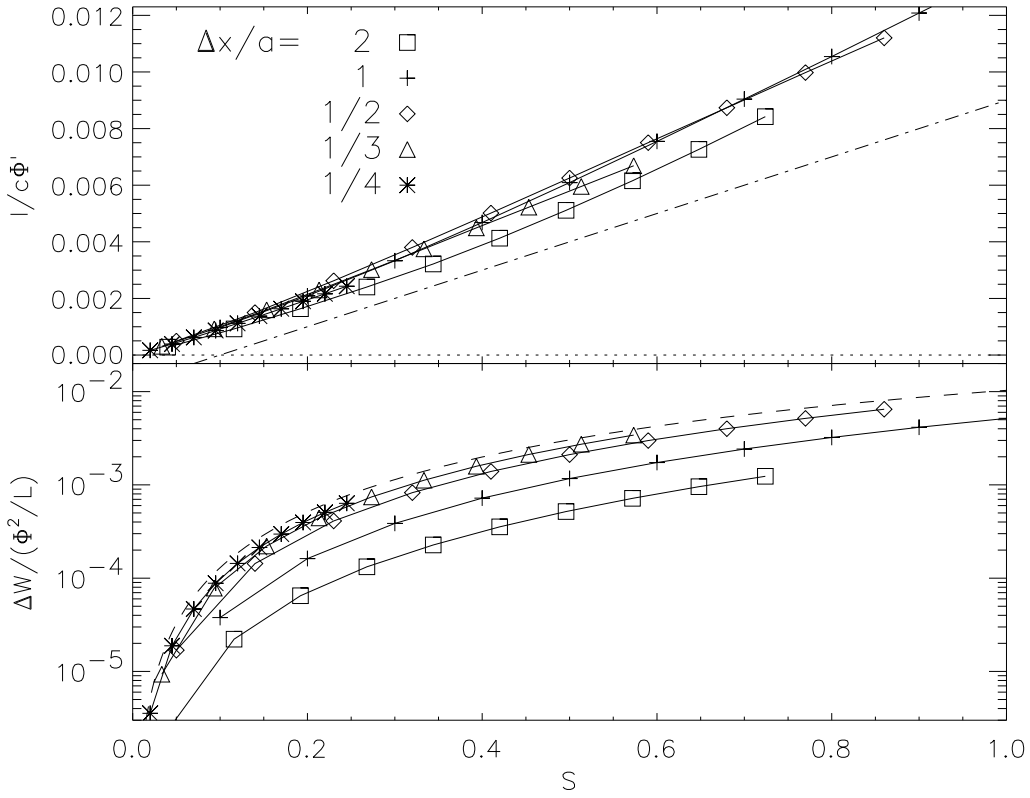

Fig. 3.— The separator current (top) and free energy (bottom) of the sheared arcade models. The two quantities are plotted against the shear parameter S for different levels of discretization Δx using different symbols listed within the top plot. A broken line in the top plot shows the curve $I/c = 10^{-2}\,\Phi'\,S$, for reference. The dashed curve in the bottom panel is the estimate of Klimchuk et al. (1988), given in Equation (1), for a value of $K = 0.75$ in the potential field (Equation [4]).

than of the point-source derived field. The former is given by expression (4) where K depends on the profile of the flux distribution. Figure 3 shows the expression with $K = 0.75$, which is a relatively small value for it.

Based on the curves in Figure 3 it seems that the MCC approximations, especially those with small $\Delta x/a$, follow the relationship of Klimchuk et al. (1988). There is a trend for the MCC energy to increase with decreasing Δx. This is natural since the finer partitioning of the flux bands provides more constraints upon the minimization, and therefore a higher energy.

The dashed curve in the lower panel of Figure 3 represents the energy stored in an MHD model with a particular photospheric flux distribution. The dependence of the potential energy on flux distribution is contained in the parameter K. The Gaussian distribution used by Klimchuk et al. (1988), $B_z(y) \sim ye^{-2y^2/a^2}$, is characterized by $K = 1$; while the Lorentzian distribution used by Choe & Lee (1996), $B_z(y) \sim y/(y^2 + a^2)^2$, corresponds to $K = \pi/4$. The former would therefore have a free energy curve higher than the dashed curve ($K = 0.75$), and so the MCC's underestimate is more conservative in the case of a Gaussian than for the case of a Lorentzian. Furthermore, distributions more tightly concentrated around the centroids, $y = \pm a/2$, have still greater potential energies but identical MCC free-energy estimates. All distributions have the same flux per axial length, Φ', which is the only characteristic used by our MCC model, since it combines an axial segment Δx long into a single source. The MCC energy must therefore be a lower bound on all of the cases, regardless of how the flux is distributed within the band.

To release any portion of this free energy it is necessary to change the connectivity of the magnetic field through magnetic reconnection. This will reduce the fluxes in some domains like $P6$–$N6$, and increase it in other like $P6$–$N7$. By so doing it will reduce the flux discrepancy, $\Psi_{6-7} - \Psi^{(\mathrm{v})}_{6-7}$, and thereby decrease the free energy. The MCC thus models the flux transfer and quantifies its energy release.

A model of these connectivity changes, including the flux rope production, requires a detailed analysis of the reconnection sequence and how it changes the topologies of the field lines. There are, however, artifacts in the topology of the infinite model, such as arbitrarily long connections in the potential field. These peculiarities are absent from an arcade extending a finite length in the erstwhile direction of symmetry. This mirrors the discrepancies between two-dimensional and three-dimensional CSHKP model discussed in the previous section. It is therefore necessary to consider topological models of finite arcades.

3. Topology of the Three-dimensional (Finite) Arcade

The finite model retains the simplicity of identical straight polarity bands separated by perpendicular distance a, but now restricted to length, L. The ratio a/L quantifies the severity of the localization in the parallel direction. Each band is partitioned as in the previous section, but since they are finite the partitioning produces $n = L/\Delta x$ sources in each band. The potential field will once again contain prone null points between every adjacent pair of sources: $2(n-1)$ null points in all.

As in the previous section, the two bands will be directly opposite each other in their initial configuration. The initial field will be a potential field and its field lines will link only those sources directly across from one another. These connections define a set of n domains, $P1$–$N1$, $P2$–$N2$ etc., we call *generation* 0.

The fan surfaces from null points opposite one another, such as $B2/3$ and $A2/3$, will coincide exactly. This topologically unstable situation is disrupted by any change which breaks the mirror symmetry, giving rise to a generic state where separatrix surfaces intersect along curves — separators. Each separator will link the two opposing nulls whose fans had previously coincided.

3.1. Potential field for case $n = 4$

Shearing the arcade distorts the field lines but does not produce any topological changes in the actual field. In contrast, the potential field does undergo topological changes as a result of shear. As just mentioned, even the smallest shearing will give rise to $n-1$ separators linking opposing null points. The slightly sheared potential field will include a new generation of domains (generation 1) linking each internal source to the opposing sources on either side of the one opposite it, such as $P2$ to $N1$ and $N3$ (see Figure 4). Sources on the ends link to the source inside the one opposite to it, such as $P1$ linking to $N2$. There are therefore $2(n-1)$ domains in the first generation. Adding these to the n domains in the zeroth generation, there are $D = 3n-2$ domains in all. This number agrees with the Beveridge-Longcope equation (Beveridge & Longcope 2005)

$$D = X + S - N_c - 1 \quad , \tag{5}$$

for $S = 2n$ sources and $X = n-1$ separators and $N_c = 0$ coronal null points.

The geometrical arrangement of the $3n-2$ domains depends on the sense of shear. A counter-clockwise shear, as in Figure 4, tilts the generation-0 domains to the left. It brings closer all opposing sources which are on the right across the PIL. The closest of these will

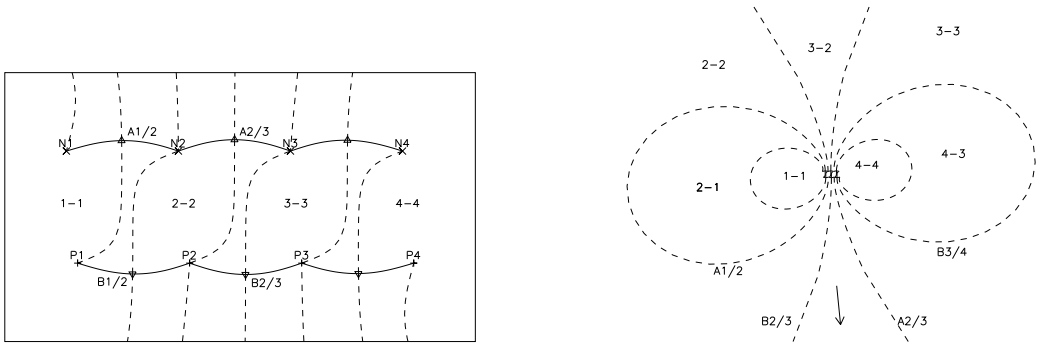

Fig. 4.— The annotated footprint of the potential field for $L = 4a = 4\Delta x$ with very small shear: $S = 0.1$. Several of the domains, Pi–Nj are labeled i–j. A few of the null points, Ai/j or Bi/j are also labeled. The right panel shows the large-scale structure of the footprint. The separatrices (dashed) are labeled by the null from which they originate. The arrow indicates the dipole moment of the sheared arcade.

be connected by a generation-1 domain whose potential flux, $\Psi^{(v)}$, must *grow* as the source approaches. This means that domains such as 1–2, 2–3, 3–4 will appear in the footprint (they are photospheric domains) and will increase with increasing shear. These $n - 1$ domains lie directly beneath the separators.

Lying above the separators are the other generation-1 domains 2–1, 3–2 and 4–3, which connect even further leftward than generation-0: they are even more sheared than generation-0. The footprints of these domains reach around the outside of the region (see Figure 4). The topology of this configuration is summarized by the left panel of Figure 5. Domains and separators of later generations are drawn with lighter lines.

The shearing changes the dipole moment of the photospheric flux distribution. It rotates the axis of the dipole in the same sense as the shear and increases its magnitude by a factor $\sqrt{1 + S^2}$. The potential field far from the arcade, dominated by the dipole moment, will therefore tend to be inclined by $\cot^{-1} S$ from the PIL. This dictates the structure of the separatrices in the far regions, as shown in Figure 4.

Increasing the shear further tilts the dipole moment of the photospheric field, and also leads to bifurcations in the topology of the potential field. For the case shown in Figure 4, ($L = 4a = 4\Delta x$) two global separator bifurcations (Brown & Priest 1999) occur at $S = 0.212$ adding new separators, we call the second generation, connecting $B2/3$ to $A1/2$ and $B3/4$ to $A2/3$. Then at $S = 0.441$ another global separator bifurcation occurs adding a third-generation separator connecting $B3/4$ to $A1/2$. The resulting field is shown in Figure 6. Each

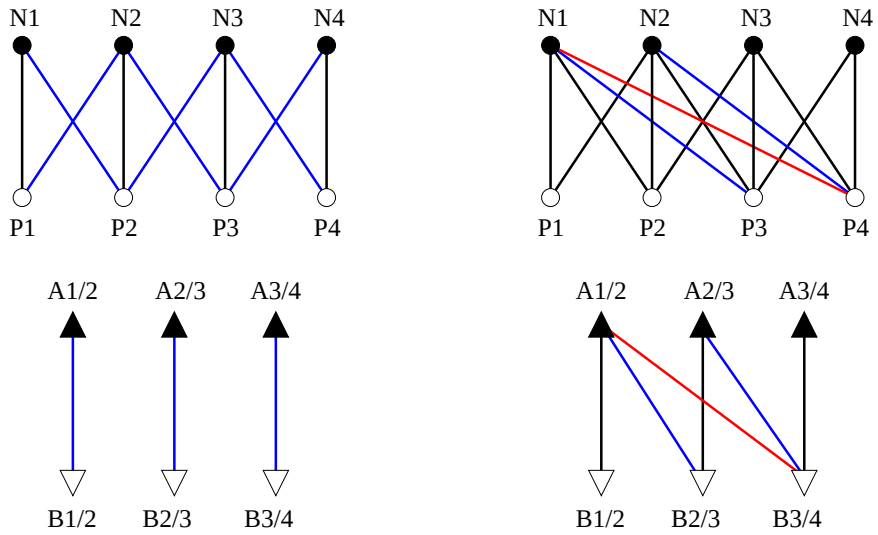

Fig. 5.— Domain graphs (top) and null graphs (bottom) illustrate the topology of the fields for the case $L = 4a = 4\Delta x$. In the domain graphs (top) vertices are sources and edges are domains linking them. In the null graphs (bottom) vertices are null points and edges are the separators linking them. The left panel is the topology of the potential field with $S = 0.1$ (see Figure 4); the right panel is $S = 0.8$ (see Figure 6). Lighter edges denote the later generations of domains (top) and separators (bottom). In the right there are two subsequent generations denoted in different shades.

subsequent generation lies above the previous one, with the single third-generation separator, σ_6 extending the highest. This tiered arrangement is also evident in the intersection in the right panel of Figure 6.

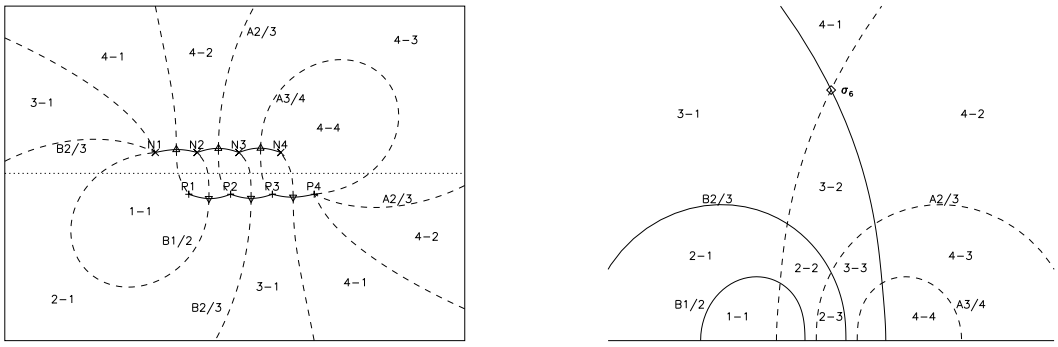

Fig. 6.— The case shown in Figure 4, at the shear of $S = 0.8$. The right panel shows the separatrices passing through a vertical plane parallel to the PIL (shown as a dotted line in the left panel). Separatrices from positive (negative) nulls are shown as solid (dashed) lines. These intersect one another at the points where separators cross the plane; the location of the third-generation separator, σ_6,is indicated by a diamond.

Each global separator bifurcation adds a new flux domain as well as a new separator, in accordance with the the Beveridge-Longcope equation (5). The first pair of bifurcations add domains 3–1 and 4–2, which are second-generation domains. The next one adds domain 4–1, the third-generation domain connecting the two most distant sources. These connections tend to extend around the outside of the arcade, and lie farther above it than the initial domains.

3.2. The general case and the limit $n \to \infty$

Models with finer partitioning, and therefore more sources, undergo a different but analogous sequence of topological bifurcations under increasing shear. The sequence begins once $S > 0$ with the first generation of separators connecting nulls directly across from each other: $B(j-1)/j$ to $A(j-1)/j$. Next a set of bifurcations creates a second generation of separators connecting nulls further left: $B(j-1)/j$ to $A(j-2)/(j-1)$. Subsequent bifurcations lead to generations of separators linking nulls even further left. Generation g links each $B(j-1)/j$ to null $A(j-g)/(j-g+1)$, providing a total of $n-g$ separators. Figure 7 shows the case with $n = 8$ sources of each sign arranged along bands $L = 4a$ long (it

is a sub-partitioning of the case from Figures 4–6). The right panel shows separatrices from positive (solid) and negative (dashed) nulls intersecting to form separators in 4 successive generations (traced by dotted curves). Separators from each successive generation lie above the preceding ones. The bifurcation sequence ends after $n-1$ generations when a single separator, higher than all others, connects $B(n-1)/n$ to $A1/2$.

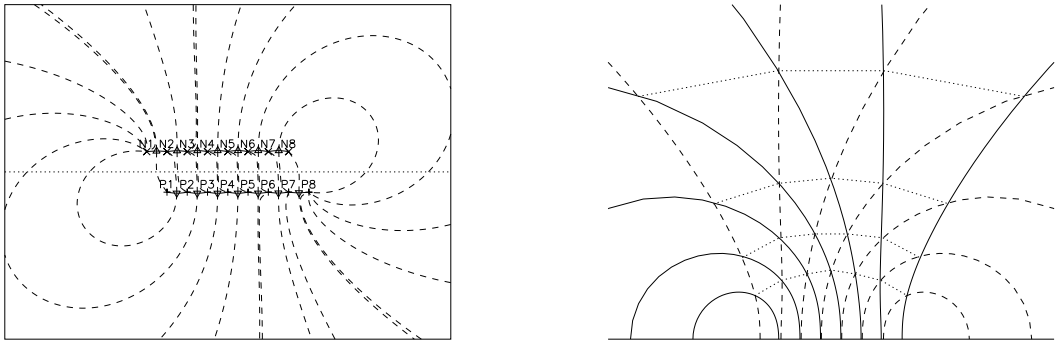

Fig. 7.— An illustration of the potential field for $n = 8$ and $L = 4a$ at shear $S = 0.5$. Both sides follow the format of Figure 6, although labels have been omitted for clarity. The right panel shows separatrices from positive (solid) and negative (dashed) lines intersecting at the location of separators. Four generations of separators are present. The separators of each generation are linked by a dotted curve. Seven separators from generation 1 are the lowest, four from generation 4 are the highest.

Each new separator, from a generation after the first, accompanies a new domain linking a source further left across the PIL. Domains from generation g link Pj to $N(j-g)$, as illustrated in Figure 8. This is true of the first generation as well, but in that case there is also a new domain linking rightward, from Pj to $N(j+1)$ (denoted R on Figure 8). All other domains link leftward and each later generation makes a smaller angle θ with the PIL. The line between source regions of a generation-g domain makes an angle whose cotangent is

$$\cot\theta_g \;=\; S + \frac{g}{n}\frac{L}{a} \quad . \tag{6}$$

The actual field lines in the domain may cross the PIL at a different angle, but this is the average angle of each complete field line. The zeroth generation crosses at $\theta_0 = \cot^{-1} S$, which is the angle of the photospheric shear. Flux from later generations crosses at an angle even more sheared than this: $\theta < \cot^{-1} S$. The final domain, created in generation $g = n-1$, is the most sheared since it connects $P(n-1)$ with $N1$.

It might appear counter-intuitive that high-lying coronal domains are sheared even

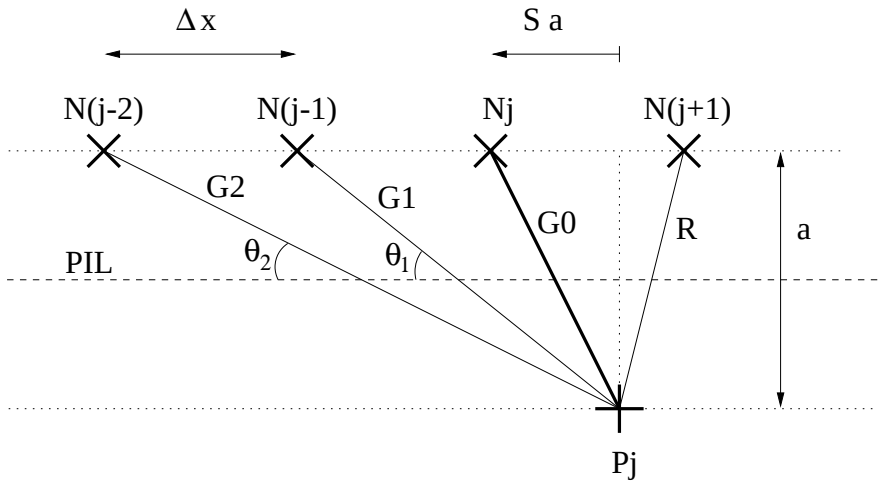

Fig. 8.— An illustration of the connections made from an arbitrary positive source Pj to negative sources to the left by domains form generations,0, 1 and 2. A second connection from generation 1, labeled R connects rightward. Each successive generation makes a smaller angle, θ_g, with the PIL (dashed).

further than the photosphere driving them. We are considering, however, the potential field, dominated at great distances by a dipole moment changing in same sense as the shear. Furthermore, the sources at the far ends of the polarity bands, for example $P4$ and $N1$ in Figure 6, deprived of connections to their nearest neighbors, are forced to connect further and further backward.

Bifurcations occur at different shears depending on the particular configurations. In a series of configurations with $L/a = 4$ fixed, but $n = L/\Delta x$ increasing, the first bifurcation occurs at smaller and smaller shear. Plotting the shear of the bifurcations against the value of $\cot\theta_g$ of the domains they create (Figure 9), shows a limiting behavior as $\Delta x \to 0$. For larger values of n (smaller Δx) early generations involve several bifurcations at closely spaced shears. The left-most point in the generation, marking the onset of that generation, fits the empirical relation

$$\cot\theta \;\simeq\; S + \frac{8S}{\sqrt{1+4S^2}} \quad . \tag{7}$$

One consequence of this limiting behavior is that even a continuous photospheric flux distribution ($\Delta x \to 0$) involves potential field lines connecting at angles much more sheared than the shear angle.

The flux of each domain can be calculated using a Monte Carlo method (Barnes et al. 2005) tracing random field lines. Domains making angles between perpendicular ($\cot\theta = 0$) and the shear angle ($\cot\theta = 0.8$) contain the majority of the flux (see Figure 10). Generations

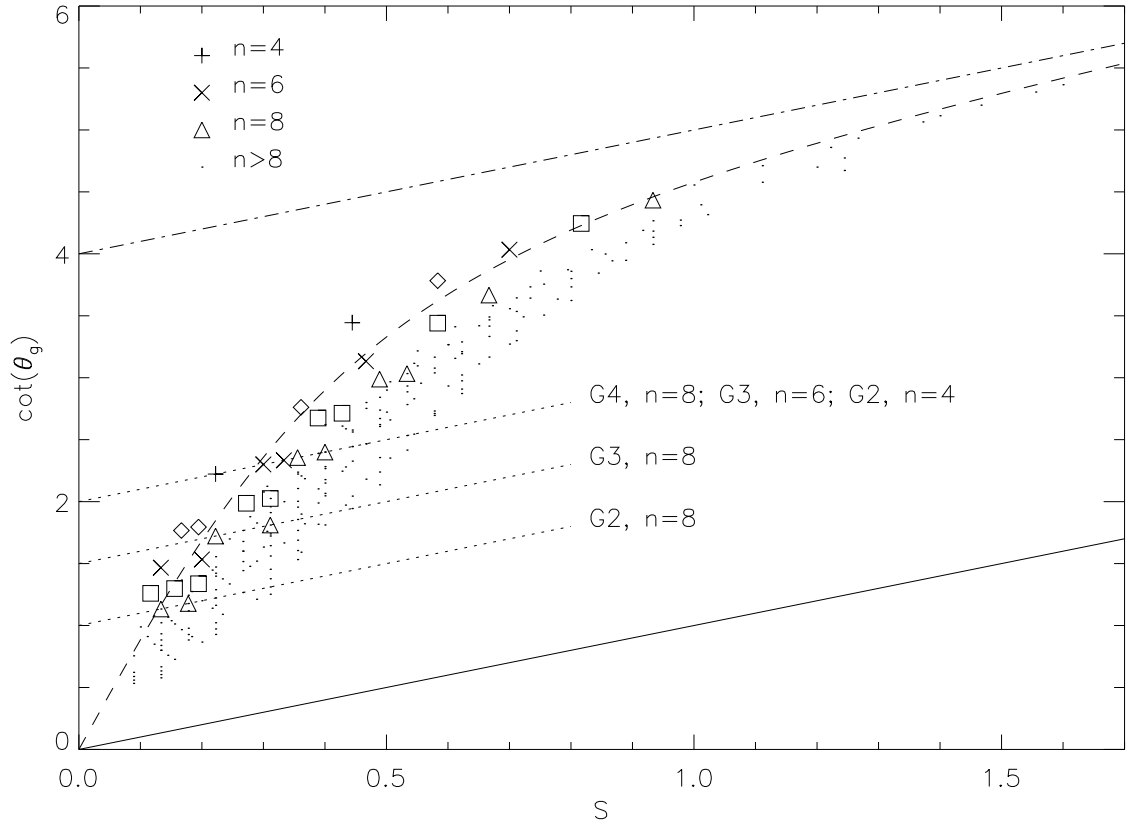

Fig. 9.— A plot of $\cot\theta_g$ for each domain created by a bifurcation as a configuration, with $L = 4a$, is sheared. Plotted are cases from $n = 4$ (+) to $n = 18$. Cases below $n = 9$ are given different symbols, while those $n \geq 9$ are plotted as dots. Empirical relation, (7), is plotted as a dashed line. The photospheric shear, $\cot\theta = S$ (the angle of generation 0) is plotted as a solid line. The dot-dashed line designates the maximum value, $\cot\theta = 4 + S$, corresponding to a connection between the two ends of the arcade in the limit $n \to \infty$.

2 and 3, of the $n = 4$ model, are more parallel to the PIL, and these do contain significant flux. This distribution persists in models with finer resolution (i.e. larger $n = L/\Delta x$), although more generations permit more possible angles and distributions with smaller stair steps. In all cases roughly 25% of the flux is at angles more sheared than the photospheric shear level. The distribution decreases steadily from $\cot\theta = S = 0.8$ to $\cot\theta = 4.2$, the limit, according to Equation (7), of domains created by bifurcation. Thus the more recently created domains have less flux, even for larger values of n, where more bifurcations have created more domains. The continuum limit, $\Delta x \to 0$, will have a continuous distribution, presumably with a similar shape.

The flux distributions plotted in Figure 10 are those of the potential field. The actual field, subject to line-tied boundary conditions, will have a distribution strongly peaked around $S = 0.8$. This discrepancy in field line mappings will store free energy in the magnetic field. This energy can be released by reconnection which creates new field lines with shear angles both less and greater than S. This reconnection will transfer the majority of the flux into less sheared domains ($\cot\theta < S$) but will also transfer some flux (approximately 25% in the present case) into domains with *more* shear. Both the increase and decrease of shear liberates energy.

4. Energetics and Reconnection

4.1. Energy and Helicity Storage

The foregoing has shown how shearing the photospheric flux bands creates, in the potential field, new domains with growing fluxes. In spite of this, the actual field consists of only the zeroth generation domains, whose field lines are simply stretched by the shearing. An estimate of free magnetic energy stored by this stretching can be obtained from a Flux Constrained Equilibrium (FCE) in which all domains have zero flux except those in the zeroth generation (these have $\Psi_i = \psi_0 = \Phi'\Delta x$).

Constraining all domain fluxes is equivalent to placing constraints on the fluxes, ψ_σ, enclosed by each of the field's separators (Longcope 2001; Longcope & Klapper 2002). The difference between the potential field and the actual field is therefore quantified by the set of separator flux discrepancies $\Delta\psi_\sigma = \psi_\sigma - \psi_\sigma^{(\mathrm{v})}$. These are listed, in Table 1, for each of the six separators present at $S = 0.8$ for the case $L = 4a = 4\Delta x$ (i.e. Figure 6). Field passes through all separators in the reverse sense (using the right-hand rule along the separator field line) making $\psi_\sigma < 0$. The separators enclose less flux (in an absolute sense) than they would in the potential field ($|\psi_\sigma| < |\psi_\sigma^{(\mathrm{v})}|$), so their discrepancies are all positive.

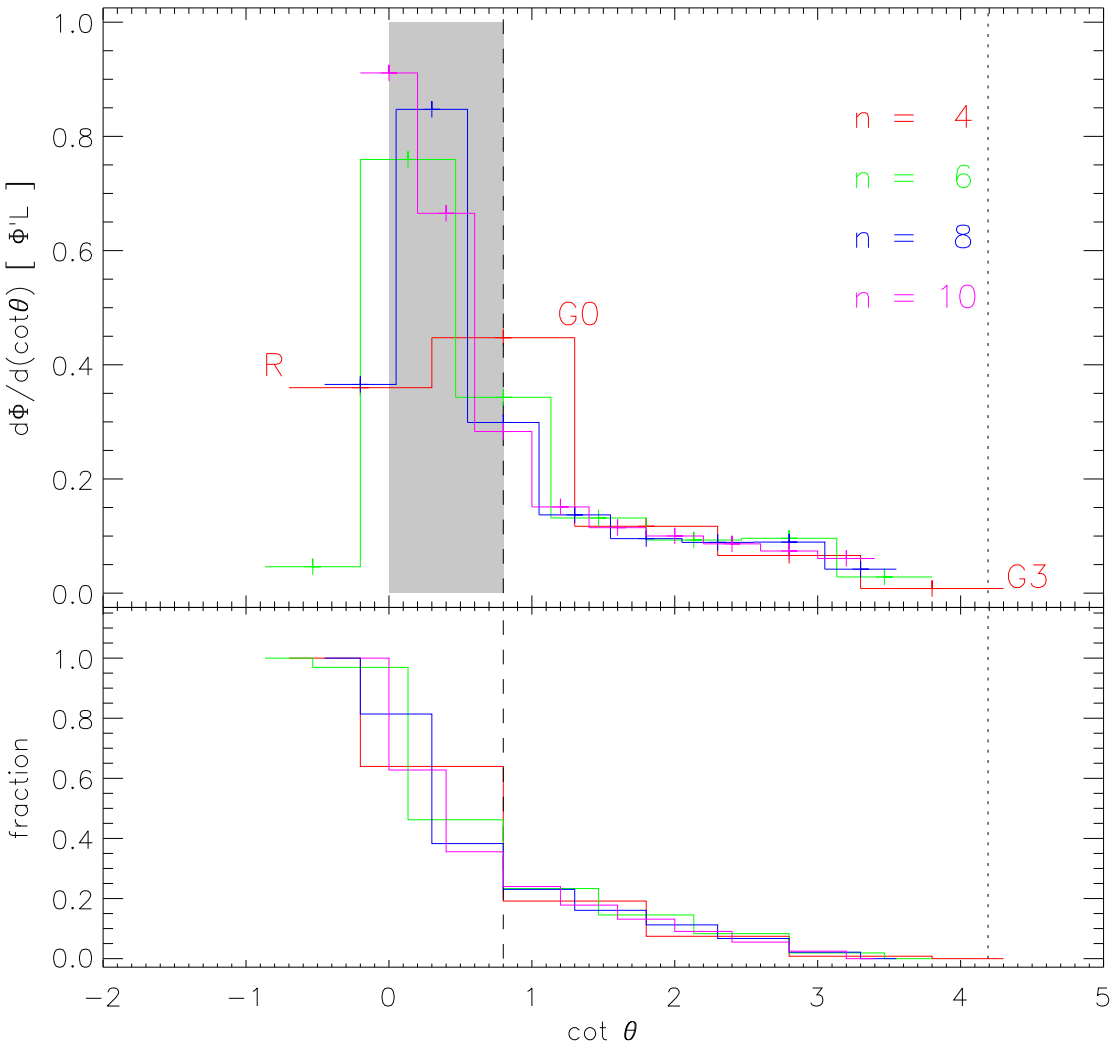

Fig. 10.— The distribution of fluxes versus footpoint angle in potential fields from various models (i.e. values of $n = L/\Delta x$) of the $L = 4a$ arcade sheared to $S = 0.8$. (Top panel) The distribution function of flux *vs.* $\cot\theta$. Each level represents a single generation, of which a few are labeled for the $n = 4$ (red) case. The region between no shear and the photospheric shear, $0 \leq \cot\theta \leq S$, is shaded. The empirically derived limit of bifurcation, Equation (7), is denoted by a dotted line. (Bottom panel) the cumulative distribution function.

σ	nulls		L_σ	$z_{\max}$	$\Delta\psi_\sigma$	I_σ/c	ΔW_σ	H_σ
	+	−	$[a]$	$[a]$	$[\psi_0]$	$[\psi_0/a]$	$[\psi_0^2/a]$	$[\psi_0^2]$
1	B1/2	A1/2	3.91	1.46	0.45	0.036	0.00565	0.437
2	B2/3	A2/3	4.41	1.68	0.51	0.038	0.00684	0.554
3	B3/4	A3/4	3.90	1.46	0.45	0.036	0.00565	0.437
4	B2/3	A1/2	7.86	2.97	0.28	0.005	0.00032	0.108
5	B3/4	A2/3	7.85	2.96	0.28	0.005	0.00032	0.108
6	B3/4	A1/2	16.00	6.20	0.12	-0.001	0.00005	-0.045
total					2.088		0.0188	1.5980

Table 1: Summary of the properties of all six separators in the field from $L = 4a = 4\Delta x$ at shear of $S = 0.8$ (the same as Figure 6). Horizontal lines group the separators into generations, 1, 2 and 3, from top to bottom.

The separator flux discrepancies will increase as the arcade is sheared, reflecting the extent to which it is driven away from potential. The top panel of Figure 11 shows the sum of the discrepancies versus S for the above case. The flux discrepancies of first-generation domains alone (labeled $G1$) appear to scale linearly with S. The other generations scale similarly, but only after their introduction by bifurcation at $S = 0.212$ ($G2$) and $S = 0.441$ ($G3$). The values relevant to $S = 0.8$, corresponding to Table 1, are indicated by diamonds.

The FCE is the magnetic field with minimum energy subject to constraints on all of its flux domains. Such a field will have current sheets on all of its separators, due to the constraints placed on the fluxes they enclose. The set of discrepancies $\Delta\psi_\sigma$ determines the currents, I_σ, carried by the separators according to the equation

$$\Delta\psi_\sigma \;=\; L_\sigma \left(\frac{I_\sigma}{c}\right) \ln\left(\frac{I^\star}{|I_\sigma|}\right) + \sum_{\rho\neq\sigma} M_{\sigma\rho}\frac{I_\rho}{c}, \tag{8}$$

where L_σ is the separator's length, $M_{\sigma\rho}$ is the mutual inductance and $I^\star_\sigma$ is the fiducial current, proportional to the average perpendicular magnetic shear in a potential field along the separator (Longcope & Magara 2004). The solutions for $S = 0.8$ are given in a column of Table 1. The flux discrepancies are all positive so, if not for effects of mutual inductances, all currents would be positive too: parallel to the separator field lines. Mutual inductive coupling, principally between separators sharing a common null (such as σ_1 and σ_6), drive negative current in the last-generation separator, σ_6.

The separator currents account for the field's free magnetic energy, which can be ap-

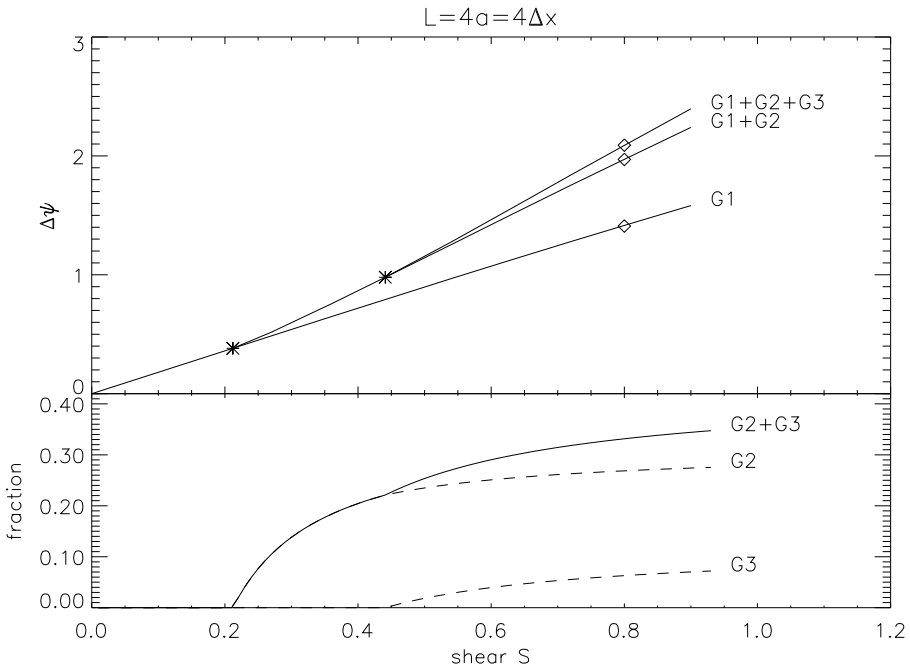

Fig. 11.— Total reconnected flux as a function of shear S. (Top) The sum of all separator flux discrepancies $\Delta\psi = \sum_\sigma |\Delta\psi_\sigma|$. The bottom curve, labeled $G1$, includes only first generation separators. The next higher curves include the second and third generation separators. These generations are created by bifurcations at $S = 0.212$ and $S = 0.441$, marked by asterisks. Diamonds mark the values at $S = 0.8$ corresponding to Table 1. (Bottom) The fraction of total reconnected flux, $\Delta\psi$, from later generations. Dashed lines are second and third generations (as labeled), the solid is their sum.

proximated (Longcope & Silva 1998; Longcope & Magara 2004)

$$\Delta W \;=\; \sum_\sigma \tfrac{1}{2} L_\sigma \left(\frac{I_\sigma}{c}\right)^2 \ln\left(\frac{e^{1/2} I^\star}{|I_\sigma|}\right) + \sum_{\sigma\neq\rho} M_{\sigma\rho}\frac{I_\sigma I_\rho}{c^2} \;=\; \sum_\sigma \Delta W_\sigma + \sum_{\sigma\neq\rho} M_{\sigma\rho}\frac{I_\sigma I_\rho}{c^2} \quad . \quad (9)$$

For the values in Table 1, the total free energy is $\Delta W = 0.023\,\psi_0^2/a$. The current on separator σ contributes to ΔW in Equation (9) a term ΔW_σ, which we designate its *self-energy*. The self-energy of each separator is listed in Table 1 as is their sum, $0.019\,\psi_0^2/a$, at the bottom. The total energy is slightly greater than the sum of self-energies due to the additional contribution of mutual inductance to ΔW.

The mutual inductance is approximated using the Neumann formula for infinitesimal wires (Griffiths 1999), which therefore does not account for the width of the current sheets. This approximation is reasonable when the two separators remain a significant distance apart, such as σ_1, σ_2 and σ_3, but is likely to overestimate the mutual inductance of separators in contact with one another, for example at a shared null point. To mitigate this overestimation we adopt the expedient measure of limiting each mutual inductance to a fraction of the smaller of the self-inductances (i.e. the lengths). The motivation for this is that the current on separator σ cannot contribute more flux to a distant separator than it does to itself. We adopt the conservative limit of 20% of its self-flux.

The top panel of Figure 12 shows the energy estimate made using this method (solid) along with several alternatives. The top curve (broken curve with a square) omits $M_{\sigma\rho}$ altogether in Equations (8) and (9). The bottom line (broken curve with a diamond) uses only first-generation separators (σ_1, σ_2 and σ_3) on whose mutual inductance no limit is applied, since they are not in contact. This version is similar to the calculation from §2, for the infinite arcade. The dashed line (with a triangle) uses the adjusted mutual inductance matrix in Equation (8) for the current, but omits it from the energy. This is equivalent to summing only the self-energies from Table 1 so the triangle corresponds to the value from the bottom line. These comparisons reveal that the effect of mutual inductance is to reduce the currents in Equation (8) but then to augment their contributions to the energy in (9). The overall effect on the energy seems to be about 20%.

It is difficult to make a direct comparison of this three-dimensional configuration to energies of analytic, two-dimensional systems, such as Equation (1) or Figure 3, since these apply to infinitely long arcades. Multiplying the analytic expression, Equation (1) for free energy per unit length by a length $L = 4a$ yields the dotted line in Figure 12. This is $\Delta W \simeq 0.028\,\psi_0^2/a$, at $S = 0.8$ (after adopting $K = 0.75$). The fact that the finite-length arcade has free energy 20% lower than this can be attributed to its field falling off in all three directions, rather than just the two possible for the infinite arcade. Only the inclusion

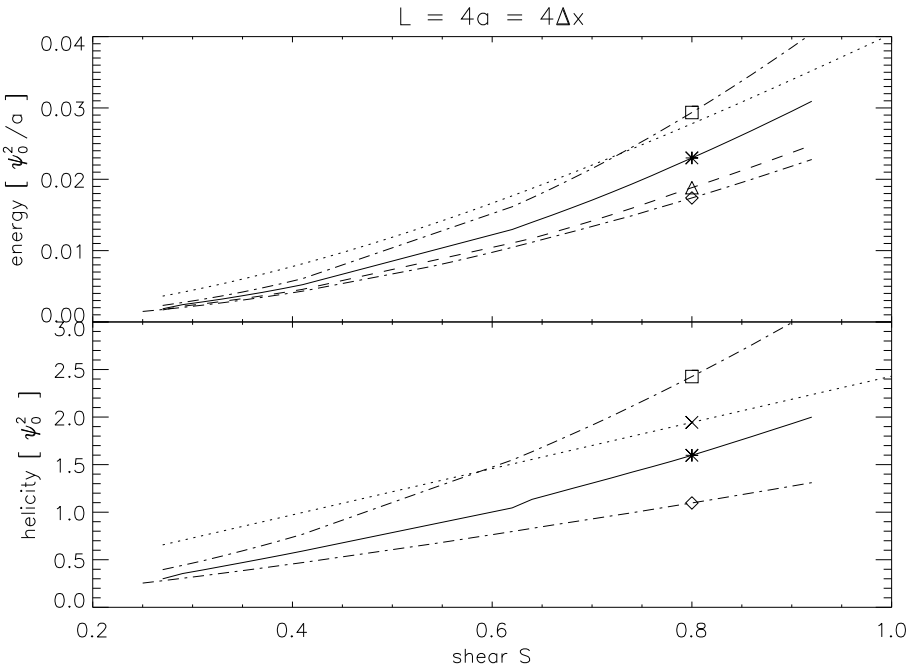

Fig. 12.— Magnetic energy (top) and helicity (bottom) of the sheared arcade model with $L = 4s = 4\Delta x$ versus the shear parameter S. Curves show versions under different treatments of the mutual inductance. A mutual inductance limited to 20% of the self-inductances (solid with asterisk), no mutual inductance (broken with square) and first-generation separators (broken with diamond). The top panel also includes the self-energies only (dashed with triangle) of the currents found with limited mutual inductances. The dotted line in the top panel is the analytic approximation, (1), multiplied by L; in the bottom panel it is the helicity injected by source region motion. Symbols occur at $S = 0.8$ corresponding to the values from Table 1.

of mutual inductances keeps the energy estimate below the two-dimensional curve; they also give the estimate a similar shape.

4.2. Helicity

The currents also produce, in the FCE field, a relative magnetic helicity (Berger & Field 1984). Relative helicity is defined to be zero for a potential field, so to lowest order its value will be proportional to the separator currents. The first-order approximation is (Longcope & Magara 2004)

$$H_R^{(\mathrm{FCE})} \simeq \sum_\sigma 2I_\sigma \int_\sigma \mathbf{Z}_p \cdot d\mathbf{l} \;=\; \sum_\sigma H_\sigma, \tag{10}$$

where $\mathbf{Z}_p$ is an auxiliary field defined so that $\nabla \times \mathbf{Z}_p = \mathbf{A}_p$, the vector potential of the potential field (Longcope & Magara 2004). The helicity of the FCE is shown as a solid line in the bottom panel of Figure 12. Once again, alternative treatment of mutual inductances (broken lines) result in modest variation.

Each term in the helicity, Equation (10), is listed in Table 1 for the shear $S = 0.8$. Each term has the same sign as its current — the typical situation. This is natural since I_σ is defined to be positive when it flows in the same direction as the magnetic field.

It is also possible to calculate the relative helicity injected into the coronal field by motions of the photospheric sources. If each source moved rigidly, without rotation, and all footpoints remained fixed within it, the coronal field would have relative helicity

$$H_R \;=\; -\frac{1}{2\pi}\sum_{a\neq b}\Phi_a\Phi_b\Delta\theta_{ab} \quad , \tag{11}$$

where Φ_a is the signed flux of source i and $\Delta\theta_{ab}$ is the net change in the angle between sources a and b. This is plotted as the dotted line in Figure 12. This simple shear injects a helicity $H_R = 1.96\,\psi_0^2$ by the time being considered ($S = 0.8$). It seems that the FCE contains about 80% of this amount. The discrepancy may be attributed to artificial footpoint motions internal to source regions, required to maintain the field in the FCE. In this sense $H_R^{(\mathrm{FCE})}$ is the *mutual* helicity implied by the interwinding of the different the flux domains; the discrepancy comes from the lack of *self*-helicity in the FCE field (Longcope & Magara 2004; Beveridge & Longcope 2006).

4.3. Reconnection

In order to release the free energy of the FCE it is necessary to violate the flux constraints by transferring flux between domains. This is accomplished by an electric field parallel to the separator field line. Each separator adjoins four domains. An electric field along it will reduce the flux in two domains, called *donors*, and increase the flux in the other two, called *recipients*. The combination of separators in the arcade configuration leads to a situation where one domain can serve as a recipient for one separator while it serves as a donor for another. The complete relaxation to a potential field will thus proceed through multiple flux transfers which must occur in a specific order.

The total amount of flux which must be transfered by reconnection, found by summing up all the flux discrepancies in Table 1, is $\sum \Delta\psi_\sigma = 2.09\psi_0$. Assuming that flare ribbons trace the field as it is reconnected, this is the value probably most closely related to observational value of ribbon-swept flux. The zeroth generation domains, on the other hand, have a total of $2.26\psi_0$ in the potential field — flux that was never reconnected. The sum of these two fluxes, $4.35\psi_0$, exceeds the total flux in the entire arcade $n\psi_0 = 4\psi_0$. The reason for this is that some flux, as much as $0.35\psi_0$, is multiply counted, as it undergoes multiple reconnection passing to a recipient who then becomes a donor.

The inter-relation of donor and recipient domains is summarized in the schematic diagram of Figure 13. Domains (circles) are connected by lines to separators (vertices) in sets of four. The two recipients are located on opposite sides of a given separator from each other, as are the two donors. The domains are arranged in the diagram so that all domains connected to a particular source form a single diagonal; a few of these are labeled. Domains from a given generation fall in a single column. Arrows along the connecting line indicate the direction of flux transfer and numbers in the circle give its flux in units of ψ_0. The top number is the flux in the initial domain while the bottom is the flux in the potential field. Complete relaxation, to a potential field, requires a flux transfer equal to the difference between the top and bottom values. A number to the upper right of each vertex indicates how much transfer would occur at that separator to accomplish this complete relaxation.

Examination of Figure 13 reveals that reconnection cannot begin on separators from generations 2 or 3 (i.e. σ_4, σ_5 or σ_6) since their donors have $\Psi_i = 0$ initially (the top number in their circle). So the first phase of reconnection must occur at the generation-1 separators, σ_1, σ_2 and σ_3. This will transfer flux into the low-lying R domains, like $P1$–$N2$ as well as second generation domains such as $P2$–$N1$. Only after this has occurred can transfer begin through the second generation separators to fill the second generation domains $P3$–$N1$ and $P4$–$N2$. Only when this second generation reconnection is underway, the third generation separator, σ_6, may undergo reconnection to fill domain $P4$–$N1$.

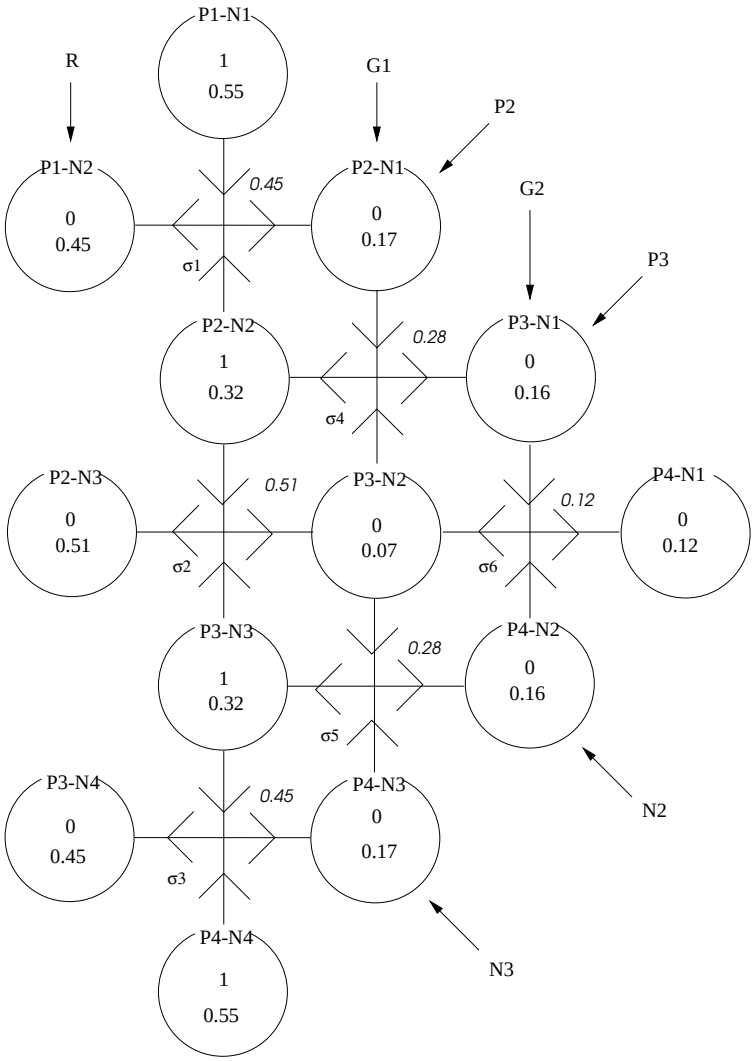

Fig. 13.— A schematic depiction of the coupling between domains (circles) by reconnecting separators (vertices). The top (bottom) number in each circle indicates its flux, in units of ψ_0, before (after) reconnection. Arrows on the lines connecting the circles to the vertices indicate the sense in which flux is transfered. A number to the upper left of the vertex lists the flux discrepancy, $\Delta\psi_\sigma$ of that separator.

In the scenario just outlined, reconnection appears to "propagate" upward even though we have not considered motion of the separators themselves. Instead we simply note that later generations extend higher into the corona and cannot undergo reconnection until their predecessors have. This progressing wave of reconnection creates field lines which are both higher and more sheared, even though they are potential. The final stage in the reconnection process creates domain $P4$–$N1$, overlying the entire arcade and connecting the two outlying ends of the polarity bands. This resembles the flux rope created in the model of Gosling (1990). We show below that the reconnection process will also endow the flux rope with significant internal twist.

Successively higher separators are longer and include less flux (see Table 1). As a result later and later reconnection liberates less and less energy. Furthermore, the higher domains consist of much longer field lines and enclose much more volume. The domains in generation-R, such as $P1$–$N2$, have field lines averaging $\langle L \rangle \simeq 1.5\,a$ and volume $V \simeq 0.7\,a^3$. The other recipient domains from first-generation reconnection, such as $P2$–$N1$ have $\langle L \rangle \simeq 9a$ and volumes as great as $V = 100\,a^3$. The lower-lying and less sheared domains will therefore accommodate liberated energy in a far smaller volume, leading to bright, dense post-reconnection loops just over the PIL. According to the model there is just as much magnetic flux in higher, weaker magnetic loops, but energy deposited onto that flux will be one hundred times more dilute.

4.4. Helicity Transport and Flux Rope Creation

Once reconnection has eliminated the flux constraints on the first-generation separators, the field may relax to a state of lower magnetic energy. This is not the state of lowest possible energy, a potential field, since there are still constraints on the three remaining separators, σ_4, σ_5, σ_6. The flux discrepancies $\Delta\psi_\sigma$ on these three are the same as in the pre-reconnection case. Absent mutual inductive couplings to σ_1, σ_2 or σ_3, however, the currents are different in this less constrained state (see Table 2). All separator currents are now positive and the second-generation currents are twice as great as before the reconnection. It seems that first-generation reconnection is the primary source of energy release, since the free energy remaining after it finishes is an order of magnitude smaller (it is $\Delta W = 0.0026\,\psi_0^2/a$ when the mutual inductance is included).

Reconnection along the second-generation separators will leave intact only the flux constraint on σ_6. This least-constrained case has free energy of $\Delta W = 1.1 \times 10^{-4}\psi_0^2/a$ and relative helicity, $H_R^{\rm FCE} = 0.074\psi_0^2$. The helicity is the mutual helicity of domain $P4$-$N1$ about the remaining flux.

σ	nulls		L_σ	$z_{\max}$	$\Delta\psi_\sigma$	I_σ/c	ΔW_σ	H_σ
	+	−	$[a]$	$[a]$	$[\psi_0]$	$[\psi_0/a]$	$[\psi_0^2/a]$	$[\psi_0^2]$
4	B2/3	A1/2	7.86	2.97	0.28	0.0107	0.00116	0.234
5	B3/4	A2/3	7.85	2.96	0.28	0.0107	0.00116	0.234
6	B3/4	A1/2	16.00	6.20	0.12	0.0011	0.00003	0.036
total					0.673		0.0024	0.5031

Table 2: Properties of second and third generation separators after reconnection has eliminated the currents on the first-generation separators.

It is thought that fast magnetic reconnection cannot significantly change the relative helicity of a field as a whole (Berger 1984). In light of this it would seem that the field could not relax from the state summarized in Table 1 to the one in Table 2, since they have different relative helicity. These helicity values represent, however, mutual helicity, so the reconnected domains would need to retain the difference, $1.1\psi_0^2$, in the form of self-helicity. We assume that this is divided between the 6 recipient domains in some ratio. A simple *ad hoc* prescription is to distribute the self-helicity in proportion to the fluxes they receive: $0.20\psi_0^2$ in $P2$–$N3$ and $P3$–$N2$ and $0.18\psi_0^2$ in all others.

These self-helicities will affect the configuration of the post-reconnection field and will be passed along through subsequent reconnection. Due to their self-helicity, the low-lying field in domains such as $P1$–$N2$ will be internally twisted. The total twist can be estimated as $\Delta H/\Psi_{1-2}^2 = 0.89$ turns. Thus the arcade formed by reconnection retains shear. Indeed, the pre-flare arcade as whole contained $1.6\psi_0^2$ in its $4\psi_0$ of flux, amounting to one tenth of a turn. Thus the reconnection actually increases the twist in the field.

The second generation reconnection will eliminate an additional $0.43\psi_0^2$ of relative helicity as it transfers flux into domains $P3$–$N1$ and $P4$–$N2$. Following the same *ad hoc* scheme as before this will add $0.11\psi_0^2$ of self-helicity to the $0.28\psi_0$ of flux in each of them. The donor domains in this reconnection process are, however, the first-generation domains which have their own self-helicity. Conservation of helicity suggests that this self-helicity will be passed along, in some proportion, with the flux. Assuming that a fraction of self-helicity equal to half the flux ratio is passed along, each domain will receive $0.11\psi_0^2$ of additional self-helicity. These smaller, second-generation domains will therefore include helicity totaling $0.22\psi_0^2$ from both generations of reconnection. They will be twisted $\Delta H/\Psi^2 = 2.86$ turns.

This brings us to the third-generation domain, $P4$–$N1$, which will contain half of the remaining mutual helicity ($0.04\psi_0^2$) plus a fraction of self-helicity from both donor domains ($0.045\psi_0^2$ from each) for a total of $0.14\psi_0^2$ of self-helicity. Accommodating this modest self-helicity in the domain with $\Psi_{4-1} = 0.12\psi_0$ flux, leads to field lines with 10 turns.

This final domain of highly twisted flux will form the flux rope overlying the arcade. It connects opposite ends of the opposing polarity bands and is therefore roughly parallel to the PIL. It is extremely twisted because it was created through a process of three successive reconnections. The flux in the domain, roughly speaking the axial flux of the flux rope, is significantly smaller than the sum of all reconnection which occurred during its production. Much of that reconnection served to create the shorter, less sheared field lines in the R-domains, such as $P1$–$N2$; this was the principle means of liberating energy. A natural by-product of this reconnection was a set of overlying domains, including the flux rope.

5. Discussion

Our topological model begins with a partitioning of the photospheric flux bands of the arcade. The arcade is sheared by moving the resulting source, thereby storing free energy in the magnetic field which we bound using the MCC. We considered arcades which were infinite or had a finite length, typically four times their width, and considered modest degrees of shear $S \leq 1$. The arcade expands only slightly within this shear regime (Klimchuk et al. 1988), so the shapes of the field lines are well approximated by those of the potential field.

The free energy estimates for the infinite arcade agree well with the analytic expression of Klimchuk et al. (1988), which is our Equation (1). The agreement is better with finer partitioning (i.e. smaller $\Delta x/a$). The limit $\Delta x \rightarrow 0$ will produce continuous flux bands of negligible width. Based on the convergence observed in our numerical experiments we expect the limiting free energy to approximate expression (1) with a potential energy given by (4) with $K \simeq 0.75$. Flux bands of width $\delta \ll a$ will actually have a potential energy characterized by $K \sim \ln(a/\delta) \gg 0.75$, so the MCC free energy is a very conservative lower bound to this case. This is natural, since the same model must apply equally to bands of non-negligible width such as the Gaussian and Lorentzian profiles used in MHD investigations of Klimchuk et al. (1988) and Choe & Lee (1996). The experiments we actually performed, down to $\Delta x = a/4$, place reasonable lower bounds on the energies of all such profiles.

It is only with an arcade of finite length that we are able to analyze the topology of the potential magnetic field. This topology is significant because the potential field is the state of lowest energy to which the stored energy must be compared. We find that it contains field lines of reduced shear ($|\cot\theta| < S$) as well as *increased* shear. Relaxation of the sheared arcade, through reconnection, will create field lines of both kinds.

The topology of the potential field changes under photospheric shearing. This change occurs, as must any topological change, through bifurcation. Here the bifurcations are of the

global separator type (Brown & Priest 1999), which create new separators and new domains in equal numbers. The bifurcations occur at different shears depending on the partitioning, so they are not significant in and of themselves. Their occurrence forms a pattern, persistent independent of partitioning, of creating later generations of more sheared domains. These domains then increase in flux under continued shearing. Field lines in the more sheared domains lie well above and around the core of the arcade. The field of the actual sheared arcade lacks such field lines since it consists of only one type of connection, which we call generation zero. It is this lack of other connections that causes the sheared arcade to have free magnetic energy.

In order to release the free energy of the sheared arcade it is necessary to populate the domains of later generations, through separator reconnection. We use a diagram, Figure 13, to deduce how this reconnection must proceed. We find that reconnection occurs first at a set of separators, the first generation, lying just above the arcade. This situation resembles, to some extent, the picture of Gosling (1990), whereby reconnection occurs at multiple sites (the Xs on the right of Figure 1). A very similar picture of multi-site reconnection was proposed by van Ballegooijen & Martens (1989), as a model for the formation of a prominence. Flux transfer in a three-dimensional field must occur across a line rather than at a single point; it must occur across a separator as it does in our model.

In our model, as in those of Gosling (1990) and van Ballegooijen & Martens (1989), reconnection produces low-lying field of reduced shear (generation-R) as well as field of greater shear (generation-1). Our model quantifies this flux transfer as a function of shear (see Figure 11). In an actual MHD field reconnection will be accompanied by a moving ribbon as new domains fill with flux. The photospheric flux swept up by the ribbons (Forbes & Priest 1984; Poletto & Kopp 1986; Fletcher et al. 2001; Qiu et al. 2002) provides a measure of $\sum_\sigma \Delta\psi_\sigma$ predicted by our model. Thus we propose Figure 11 as a model of the relationship between shear and reconnected flux.

After reconnection along the first generation of separators, there will be reconnection along overlying separators of later generations. In this way reconnection progresses upward even in our model which does not account for motions of the reconnection sites themselves. Each subsequent level of reconnection transfer less flux and releases less free energy than the previous one. Each new generation of field lines lies higher and makes connections which are more highly sheared. The final generation is a flux rope connecting the far ends of the flux bands, similar to the configuration proposed by Gosling (1990).

We expect the multi-stage reconnection process to endow the flux rope with a large amount of twist. Several methods have been used by previous investigators to demonstrate and quantify the creation of twist through magnetic reconnection (Wright & Berger 1989;

Song & Lysak 1989; Chae 1999; Linton & Antiochos 2002). These studies show a trend for the reconnection of two flux tubes to add an additional one-half turn to the field lines, as mutual helicity is converted to self-helicity. In our calculation we estimate the twist by assuming the mutual helicity present in the FCE was converted to self-helicity. Our method was not self-consistent since the FCE does not have any self-helicity. Nevertheless, our results are basically consistent with the previous investigations: each reconnection introduces additional twist.

We have chosen to model the large-scale magnetic field, including its response to magnetic reconnection. We have not needed to specify what mechanism is responsible for maintaining the reconnection electric field or how this process might have been triggered. Studies of the microphysics of reconnection have identified numerous mechanisms, all of which affect the the large scales in the same manner: they produce a reconnection electric field which transfers magnetic flux. The one feature we have assumed, which is present in only some microphysical mechanisms (Bhattacharjee 2004), is that fast reconnection is inactive for a long period of build-up. Were this not the case the magnetic field would have been able to relax continuously, at the same rate it was stressed; there would have been no sudden flare or eruption. Assuming this one aspect, we predict global consequences of the reconnection electric field including the total energy release and the flux rope produced.

In our model a twisted flux rope is formed *during* the flare and eruption. This contrasts with a class of models premised on the eruption of a flux rope which had existed prior to the flare (Fan & Gibson 2003; Török & Kliem 2003). Excessive twist of these pre-existing flux ropes often drives the eruption and the flare in such models, for instance through the external kink instability (Hood & Priest 1979; Linton et al. 1996). Since the flux rope produced in our model has twist well in excess of the instability threshold, kink-driven dynamics are likely to occur under the scenario proposed by our model, but this kinking cannot drive the process. The key difference then is that in our model the magnetic reconnection which releases the stored energy and produces the flare ribbons *also* creates the flux rope. This fact leads to naturally to a relationship among the shear, the reconnected flux, the twist and the axial flux in the flux rope. Figure 11 shows the form of this relationship predicted by our model.

In this work we demonstrated how the MCC reproduces known results of the CSHKP model of an idealized two ribbon flare. The same methods can be applied to predict energy storage and reconnection in actual two ribbon flare. Longcope et al. (2007) did this with 40 hours of pre-flare magnetic evolution followed by an X-class flare and CME on Nov. 7, 2004. The photospheric field in that case was naturally more complex than the two symmetric, featureless bands considered above. The photospheric motion was also more complex than a simple shear. Nevertheless, the observed motion led to changes in the domain fluxes

analogous to those just considered. These domain fluxes changes were used to estimate the free energy storage. Moreover, the observed motion injected a helicity equivalent to a shear parameter $S = 1/3$, well within the range treatable by MCC. Thus the MCC approach is capable of bridging the gap between idealized models and the complexity of actual corona fields.

A. Mutual inductance of an infinite arcade

A current I_σ flowing along separator σ will contribute flux $M_{\rho\sigma} I_\sigma$ to separator ρ. If these two separators are everywhere far enough apart, the flux contribution will not be greatly affected by the internal distribution of the current on σ. In that case the mutual inductance can be estimated using the Neumann formula (Griffiths 1999) which assumes I_σ is confined to a closed curve of infinitesimal cross section. The Neumann formal gives the mutual inductance as the manifestly symmetric double integral

$$M_{\sigma\rho} = \oint_\sigma \oint_\rho \frac{d\ell_\sigma \, d\ell_\rho \; \hat{\mathbf{t}}_\sigma \cdot \hat{\mathbf{t}}_\rho}{|\mathbf{r}_\sigma - \mathbf{r}_\rho|}, \tag{A1}$$

where $\mathbf{r}_\sigma$ is the curve of separator σ, ℓ_σ is its arclength and $\hat{\mathbf{t}}_\sigma \equiv \partial \mathbf{r}_\sigma / \partial \ell_\sigma$ is its tangent vector.

Each separator curve in our configurations begins and ends at a prone photospheric null. These open curves must be somehow closed in order to apply Equation (A1). The boundary condition that $B_z = 0$ at $z = 0$, from any separator current, is satisfied by the method of images by closing the separator along its mirror image. We designate this closed curve $\mathcal{C}_\sigma$. The similarly-constructed $\mathcal{C}_\rho$ will enclose exactly twice the flux of the actual separator, half its flux being in $z < 0$. The mutual inductance relating current I_σ to the *coronal* flux enclosed by separator ρ is therefore

$$M_{\sigma\rho} = \frac{1}{2} \oint_{\mathcal{C}_\sigma} \oint_{\mathcal{C}_\rho} \frac{d\ell_\sigma \, d\ell_\rho \; \hat{\mathbf{t}}_\sigma \cdot \hat{\mathbf{t}}_\rho}{|\mathbf{r}_\sigma - \mathbf{r}_\rho|} \quad . \tag{A2}$$

It is even evident from the form of Equation (A1) that difficulties will occur if the two separators cross, since the point they touch will have $|\mathbf{r}_\sigma - \mathbf{r}_\rho| = 0$, and the integral will diverge. An infinitesimal line current encloses an infinite amount of self-flux due to the divergence of $|\mathbf{B}|$ at the current. It will share some (finite) fraction of this with any curve which touches it, thereby leading to a diverging mutual inductance.

The actual separator currents are not concentrated into infinitesimal curves, but form sheets whose width can be estimated, using the structure of a two-dimensional current sheet (Green 1965; Syrovatskii 1971), to be

$$\Delta(\ell_\sigma) \;=\; \sqrt{\frac{4|I_\sigma|}{\pi B'(\ell_\sigma)}} \quad , \tag{A3}$$

where $B'(\ell_\sigma)$ is the magnetic shear perpendicular to the *potential field* separator line at position ℓ_σ (Longcope & Magara 2004). The width of the current increases with the current it carries. This width enters the self-inductance logarithmically, giving rise to its form: $I_\sigma \ln(eI^\star_\sigma/|I_\sigma|)$, where $I^\star$ involves a geometrical average of $B'(\ell)$ over the separator. This same finite width will prevent the divergence in $M_{\sigma\rho}$ if the denominator is limited to the larger of the two widths.

The infinite arcade is translationally symmetric so that the current on every separator is the same: $I_\sigma = I$. This means that the sum of all mutual inductive contributions becomes

$$\sum_{\rho\neq\sigma} M_{\sigma\rho} I_\rho \;=\; \left(\sum_{\rho\neq\sigma} M_{\sigma\rho}\right) I \;=\; \tilde{M} I \quad . \tag{A4}$$

Due to symmetry all separators are copies of each other translated by an integral number of intervals, Δx, along the x axis. Denoting by $M(x)$ the mutual inductance between two separated by x we can write

$$\tilde{M} \;=\; 2\sum_{j=1}^{\infty} M(j\Delta x) \quad . \tag{A5}$$

The convergence of the sum above depends on the behavior of $M(x)$ for large x. At large separations each separator will appear to the other like a dipole and

$$M(x) \simeq \frac{1}{\pi^2}\frac{L^4}{|x|^3} \quad , \quad |x| \gg L \quad ,$$

where L is the length of the separator (i.e. only the coronal portion). Thus the terms in the sum decrease as j^{-3} for large j, and the sum converges.

As a simple approximation to the infinite series (A5) we approximate each separator as a semi-circle of length L (i.e. radius L/π). The closure, $\mathcal{C}$, are therefore completes circle and $M(x)$ is the mutual inductance between two co-axial rings (Jackson 1975). The total inductive contribution then becomes

$$\tilde{M} \;=\; 2L\sum_{j=1}^{\infty} \frac{1}{k_j}\left[\,(2-k_j^2)K(k_j) - 2E(k_j)\,\right] \quad , \quad k_j \;\equiv\; \left[1+\left(\frac{j\pi\Delta x}{2L}\right)^2\right]^{-1/2} \quad , \tag{A6}$$

were $K(k)$ and $E(k)$ are complete elliptic integrals. We retain at least 30 terms of the series, beyond which we have found little change in the total. In order to account for the finite width of the current sheets we limit each term in this sum to $\ln(eI^\star/|I|)$. The term is replaced with this value in cases where $\Delta x/L$ is so small it would exceed it. Since the limit depends on the solution, the process must be iterated until a consistent solution is found. This is our process for finding I and $\tilde{M}$.

This work was supported by NSF under grant ATM-0416340.

REFERENCES

Barnes, G., Longcope, D. W., & Leka, K. D. 2005, ApJ, 629, 561

Berger, M. A. 1984, Geophys. Astrophys. Fluid Dynamics, 30, 79

Berger, M. A., & Field, G. B. 1984, JFM, 147, 133

Beveridge, C., & Longcope, D. W. 2005, Solar Phys., 227, 193

Beveridge, C., & Longcope, D. W. 2006, ApJ, 636, 453

Bhattacharjee, A. 2004, ARA&A, 42, 365

Biskamp, D., & Welter, H. 1989, Solar Phys., 120, 49

Brown, D. S., & Priest, E. R. 1999, Proc. R. Soc. Lond. A, 455, 3931

Burlaga, L., Sittler, E., Mariani, F., & Schwenn, R. 1981, JGR, 86, 6673

Carmichael, H. 1964, in AAS-NASA Symposium on the Physics of Solar Flares, ed. W. N. Hess (Washington, DC: NASA), 451

Chae, J. 1999, Journal of Korean Astronomical Society, 32, 137

Choe, G. S., & Lee, L. C. 1996, ApJ, 472, 360

Fan, Y., & Gibson, S. E. 2003, ApJ, 589, L105

Fletcher, L., Metcalf, T. R., Alexander, D., Brown, D. S., & Ryder, L. A. 2001, ApJ, 554, 451

Forbes, T. G., & Priest, E. R. 1984, in Solar Terrestrial Physics: Present and Future, ed. D. Butler & K. Papadopoulos (NASA), 35

Gosling, J. T. 1990, in Geophys. Monographs, Vol. 58, Physics of Magnetic Flux Ropes, ed. C. T. Russel, E. R. Priest, & L. C. Lee (AGU), 343

Green, R. M. 1965, in Stellar and Solar magnetic fields. Proc. IAU Symp. 22, ed. R. Lust (Amsterdam: North-Holland), 398

Griffiths, D. J. 1999, Introduction to Electrodynamics (New Jersey: Prentice Hall)

Hirayama, T. 1974, Solar Phys., 34, 323

Hood, A. W., & Priest, E. R. 1979, Solar Phys., 64, 303

Jackson, J. D. 1975, Classical Electrodynamics (New York: Wiley)

Klimchuk, J. A., Sturrock, P. A., & Yang, W.-H. 1988, ApJ, 335, 456

Kopp, R. A., & Pneuman, G. W. 1976, Solar Phys., 50, 85

Linton, M. G., & Antiochos, S. K. 2002, ApJ, 581, 703

Linton, M. G., Longcope, D. W., & Fisher, G. H. 1996, ApJ, 469, 954

Longcope, D., Beveridge, C., Qiu, J., Ravindra, B., Barnes, G., & Dasso, S. 2007, Solar Phys. (submitted)

Longcope, D. W. 1996, Solar Phys., 169, 91

Longcope, D. W. 2001, Phys. Plasmas, 8, 5277

Longcope, D. W., & Klapper, I. 2002, ApJ, 579, 468

Longcope, D. W., & Magara, T. 2004, ApJ, 608, 1106

Longcope, D. W., & Silva, A. V. R. 1998, Solar Phys., 179, 349

Mikic, Z., Barnes, D. C., & Schnack, D. D. 1988, ApJ, 328, 830

Poletto, G., & Kopp, R. A. 1986, in The Lower Atmospheres of Solar Flares, ed. D. F. Neidig (National Solar Observatory), 453

Qiu, J., Hu, Q., Howard, T. A., & Yurchyshyn, V. B. 2007, ApJ, In press

Qiu, J., Lee, J., Gary, D. E., & Wang, H. 2002, ApJ, 565, 1335

Song, Y., & Lysak, R. L. 1989, JGR, 94, 5273

Sturrock, P. A. 1968, in IAU Symp. 35: Structure and Development of Solar Active Regions, 471

Syrovatskii, S. I. 1971, Sov. Phys. JETP, 33, 933

Török, T., & Kliem, B. 2003, A&A, 406, 1043

van Ballegooijen, A. A., & Martens, P. C. H. 1989, ApJ, 343, 971

Wright, A. N., & Berger, M. A. 1989, JGR, 94, 1295